hBN layer promoted heteroepitaxy in reactively sputter-deposited $MoS_{x\approx 2}$ (0001)/Al_2O_3(0001) thin films

Aditya Deshpande[1*], *Koki Hojo*[2], *Koichi Tanaka*[1], *Pedro Arias*[1], *Hicham Zaid*[1], *Michael Liao*[1],
Mark Goorsky[1], *and Suneel Kodambaka*[1,3]

[1]Department of Materials Science and Engineering, University of California Los Angeles, Los Angeles, CA 90095, USA

[2]Graduate Department of Micro-Nano Mechanical Science and Engineering, Nagoya University, Nagoya, Japan

[3]Department of Materials Science and Engineering, Virginia Polytechnic Institute and State University, Blacksburg, VA 24061, USA

*Corresponding author

Email: adityad17@ucla.edu

KEYWORDS: molybdenum disulfide, hexagonal boron nitride, reactive sputtering, van der Waals epitaxy, buffer layers

ABSTRACT

We show that van der Waals (vdW) bonded hexagonal boron nitride (hBN) promotes heteroepitaxial growth of $MoS_x(0001)$ ($x = 2.0 \pm 0.1$) thin films on $Al_2O_3(0001)$ substrates. hBN layers are grown on $Al_2O_3(0001)$ via pyrolytic cracking of borazine (~ 6×10^4 L) at 1373 K. The MoS_x layers are deposited in an ultrahigh vacuum system via reactive direct current magnetron sputtering of Mo in Ar/H_2S gas mixture at 1073 K on bare and hBN-covered $Al_2O_3(0001)$. Using *in situ* low-energy electron diffraction and Auger electron spectroscopy along with *ex situ* X-ray diffraction, X-ray photoelectron and Raman spectroscopies, and transmission electron microscopy, we determine the as-deposited MoS_x layer composition and crystallinity. We obtain highly 0001-oriented 2H-structured MoS_x thin films with better crystalline quality on $hBN/Al_2O_3(0001)$ than on $Al_2O_3(0001)$. We suggest that hBN layers enhance surface diffusion, compared to bare $Al_2O_3(0001)$, leading to the observed improvement in crystallinity of MoS_x layers.

INTRODUCTION

The isolation of free-standing graphene layers from bulk graphite led to a surge in the discovery and synthesis of atomically thin, two-dimensional (2D) crystals of van der Waals (vdW) bonded layers. Among numerous vdW solids identified in addition to graphite, hexagonal boron nitride (hBN), and molybdenum disulfide (MoS_2), are well-known as solid lubricants. Bulk MoS_2 (molybdenite) has two naturally occurring polytypes - hexagonal structured 2H-MoS_2 ($P6_3/mmc$, a = 0.316 nm, c = 1.229 nm) and rhombohedral 3R-MoS_2 (R3m, a = 0.316 nm, c = 1.837 nm).[1–5] Bulk 2H-structured MoS_2 is semiconducting with an indirect bandgap of 1.23 eV; in contrast, a single-molecule thick 2H-MoS_2 layer has a direct band gap of 1.9 eV.[6,7] hBN ($P6_3/mmc$, a = 0.250 nm, c = 0.665 nm) is an insulator with similar thickness-dependent indirect and direct bandgaps of 5.95 eV and 6.1 eV, respectively, for the bulk and the monolayer.[8,9]

Recent studies indicate that lateral and vertical stacks of vdW materials[10–12] offer new properties and are attractive for a variety of applications including but not limited to, flexible and low-power field effect transistors, optoelectronic devices, gas sensors, twistronics, and quantum information processing.[10–15] As a result, synthesis of stacked layers of dissimilar vdW solids of desired thickness, composition, crystallinity, and relative orientation over large areas has been a key focus of the 2D layered materials community. MoS_2/graphene and MoS_2/hBN vertical heterostructures have been synthesized *via* both chemical and physical vapor deposition (CVD & PVD) methods.[16–20] In these experiments, nanometer- to centimeter-scale MoS_2 monolayer or bilayer domains were grown using ammonium tetrathiomolybdate [$(NH_4)_2MoS_4$],[16] with $MoCl_5$ or MoO_3 and sulfur as Mo and S precursors, respectively[17,18] and, *via* sulfurization of Mo in H_2S atmospheres[19,20] on CVD-grown graphene or hBN layers.

While there has been considerable interest in the synthesis of vdW multilayer stacks, relatively few studies[21] have investigated the effect of vdW layers on the growth-related aspects of overlayers. Van der Waals epitaxy, a term coined by Koma and coworkers, where heteroepitaxial growth of a vdW layer proceeds on another vdW-bonded substrate or on a 3D solid substrate (with covalent, ionic, and/or metallic bonding) and *vice versa* has been demonstrated in a variety of materials.[22–28] Koma and coworkers suggested that vdW bonding across, and the lack of dangling bonds on, the substrate surface weaken interactions between the adatoms and the substrate, enhancing the mobility of the adspecies and resulting in better crystallinity of the deposited film. Kim and coworkers have reported on remote epitaxy, where a film (e.g., GaN) grown on a covalently bonded substrate [e.g., GaN(0001)] covered with a monolayer of exfoliated graphene maintains epitaxial registry with the substrate despite the presence of the vdW layer.[29,30] With graphene as a growth template for MoS_2, an earlier study found that strain, wrinkling, and defects in the template affect the nucleation density of MoS_2 domains influencing layer coverage and large area growth.[31] Here, we focus on the growth of MoS_2 layers on hBN-covered $Al_2O_3(0001)$ [hereafter referred to as hBN/$Al_2O_3(0001)$] substrates.

In this article, we present results from the microstructural characterization of reactively sputter-deposited $MoS_{x\approx 2}$ thin films on $Al_2O_3(0001)$ and hBN/$Al_2O_3(0001)$ substrates. From X-ray photoelectron spectroscopy (XPS), X-ray diffraction (XRD), and transmission electron microscopy (TEM) data obtained from the as-deposited samples, we determine the S/Mo ratio x as 2.0 ± 0.1 and that the MoS_x layers are highly 0001-oriented with 2H-structure. Using a combination of XRD and Raman spectroscopy measurements, we show that MoS_x thin films on hBN/$Al_2O_3(0001)$ are of better crystalline quality than those grown on bare $Al_2O_3(0001)$. Our results indicate that hBN layers enhance 0001 orientated growth of MoS_x ($x = 2.0 \pm 0.1$). We suggest that hBN and possibly other vdW-bonded layers can facilitate similar improvements in crystallinity of thin films of a variety of other materials.

EXPERIMENTAL SECTION

Thin Film Deposition

All the depositions are carried out on single-side polished, 10 × 2 × 0.5 mm^3, $Al_2O_3(0001)$ substrates in a custom-built, dual-chamber, ultra-high vacuum (UHV, base pressure $< 5.0 \times 10^{-9}$ Torr, 6.67×10^{-7} Pa) system, described in Refs. [32–34]. First, the $Al_2O_3(0001)$ substrates are cut from 10 × 10 × 0.5 mm^3 $Al_2O_3(0001)$ single crystals (miscut < 0.5°, 99.99% purity, from MTI Corp.), cleaned *via* sonication for 600 s sequentially in acetone, isopropyl alcohol, and distilled water, blown dry with compressed nitrogen, and baked in air at 473 K for 12 h in an oven. Each of these substrates is mounted on a heating holder, with Mo foil as the resistive heater, described in Ref. [32], and is introduced into the UHV deposition system through the load-lock chamber, where it is held for ≈ 2700 s while being evacuated by a 66 l/s turbomolecular pump. The sample holder assembly is then transferred to the main chamber and degassed at 1273 K until the base pressure of the main chamber is $< 6 \times 10^{-9}$ Torr (8×10^{-7} Pa). The substrate temperatures T_s are measured prior to the depositions, i.e., on bare $Al_2O_3(0001)$, using an IMPAC IS-8GS pyrometer placed outside the chamber, approximately 0.4 m away from the sample. Since $Al_2O_3(0001)$ is optically transparent, we set the pyrometer emissivity to 0.15, the expected emissivity of Mo foil that is behind the substrates. In our experiments, we measure variations in T_s up to 100 K (at T_s = 1073 K) and 200 K (at T_s = 1373 K) along the length of the sample.

The CVD of hBN layers is carried out *via* pyrolytic cracking of borazine on $Al_2O_3(0001)$ at T_s = 1373 K in the same deposition chamber following the procedure described in Refs. [49,50]. First, the liquid borazine ($[B_3N_3H_6]$, vapor pressure ≈ 283 Torr (3.77×10^4 Pa) at 300 K)[51] from Gelest

Inc. is vacuum-transferred to a 20 ml UHV-compatible domed glass tube (Accu-Glass Products Inc.) and purified by freeze-evacuate-thaw cycles (Refs. [49,50]). Then, the $Al_2O_3(0001)$ substrate is exposed to ≈ 2.0×10^{-4} Torr (2.67×10^{-2} Pa) of borazine for 300 s, i.e., for a cumulative dose of 6×10^4 L, at 1373 K, after which the chamber is evacuated and the T_s set to 1073 K for the deposition of MoS_x films.

All the MoS_x films are grown on bare $Al_2O_3(0001)$ and hBN/$Al_2O_3(0001)$ substrates at T_s = 1073 K *via* dc magnetron sputtering of a 50.8 mm diameter × 3.175 mm thick Mo target (99.95% pure from ACI Alloys Inc.) in 20 mTorr Ar (2.67 Pa) with 1% H_2S gas mixture at 50 W. First, H_2S gas (99.5% pure) is introduced into the main chamber through a UHV leak valve, and its partial pressure is set to 2.0×10^{-4} Torr (2.67×10^{-2} Pa). Then, Ar gas (99.999% pure) is added through a separate UHV leak valve and the total pressure of Ar + H_2S gas mixture is adjusted to 20 mTorr (2.67 Pa). Before each deposition, the Mo target is sputter-cleaned for 120 s with the target shutter closed. MoS_x films are grown for times t = 300 and 1800 s, yielding ≈ 3 and 20 nm thick layers, respectively. (During these experiments, the target voltage varied from 292 ~ 295 V.) After the deposition, gas flow is stopped, and the samples are cooled passively to room temperature by switching off the substrate heater current. *In situ* low-energy electron diffraction (LEED) and Auger electron spectroscopy (AES) data are acquired from thinner MoS_x films and *ex situ* XRD, XPS, Raman spectroscopy, and TEM characterizations are carried out using thicker MoS_x layers as described in the following section.

Thin Film Characterization

The $Al_2O_3(0001)$ substrate, hBN layers, and ultrathin (≈ 3 nm) MoS_x films are characterized *in situ* using UHV-compatible LEED/AES hybrid system RVL2000 (LK Technologies). AES spectra are acquired in derivative mode using a 1500 eV primary beam and kinetic energies between 70 and 550 eV with a step size of 0.1 eV and a dwell time of 1 s. LEED patterns are obtained at incident electron energies between 200 and 250 eV using a screen voltage of 4 kV.

XPS characterization of an air-exposed $MoS_x/Al_2O_3(0001)$ sample is conducted in a Kratos Analytical AXIS Ultra DLD machine. High resolution S 2*p* and Mo 3*d* spectra are acquired with a step size of 0.1 eV. Binding energies are calibrated using O 1*s* peak set to 530.6 eV. We do not sputter-etch the surface to avoid preferential etching of anions (in this case, sulfur) from the film.[52–55] Spectral peak positions and integrated intensities are determined using a Gaussian function with a Lorentzian character [GL(30)] in Casa XPS software package[56] after correcting for the background based on Shirley algorithm.[57] Ratios of the integrated intensities of S 2*p* and Mo 3*d* peaks, respectively, corrected by their relative sensitivity factors 0.668 and 3.32 (from Casa XPS element library) are used to estimate the film composition.

XRD 2θ:ω scans are obtained from $MoS_x/Al_2O_3(0001)$ and MoS_x/hBN/$Al_2O_3(0001)$ using a Bede D1 high-resolution diffractometer. The samples are mounted on a miscut Si(001) wafer to eliminate background signals from the diffractometer stage. The detector and X-ray optics are aligned to achieve maximum direct-beam intensity. The sample and stage are calibrated with respect to ω and χ (out-of-plane rotation perpendicular to ω) using the Al_2O_3 0006 reflection at $2\theta = 41.68°$. 2θ:ω symmetric scans are acquired for 2θ values between 10 and 120° using double-axis diffraction with a step size of 0.02° and a dwell time of 1 s. ω rocking curves of MoS_x 0002 reflections from samples grown on $Al_2O_3(0001)$ and hBN/$Al_2O_3(0001)$ are obtained around $\theta = 7.18°$ over a range of 5.55° with a step size of 10 arcsecond and a dwell time of 1 s. 2θ:ω asymmetric scans for the $10\bar{1}3$ reflection from both samples are acquired in skew-symmetric geometry over a range of 4.5° with a step size of 0.05°, and a dwell time of 700 s. For these measurements, we use Al_2O_3 $11\bar{2}6$ reflection at $2\theta = 57.52°$ as reference.

Two sets of Raman spectra are acquired at room temperature from the $MoS_x/Al_2O_3(0001)$ and MoS_x/hBN/$Al_2O_3(0001)$ thin films using a Horiba LABRAM HR Evolution Confocal Microscope system equipped with a 532 nm wavelength laser at 0.6 mW power (and a Renishaw In-Via Raman Confocal Microscope system equipped with a 633 nm laser at 0.4 mW), over 100 cm^{-1} – 1800 cm^{-1} (100 cm^{-1} – 1500 cm^{-1}) spectral range with 0.5 cm^{-1} (2 cm^{-1}) resolution. Laser spot sizes for both sets of measurements are 1 μm. Prior to each measurement, the instruments are calibrated using a Si substrate with a known Raman peak of 520.1 cm^{-1}. The MoS_x samples are then placed on the stage and Raman spectra are obtained from regions of interest identified using an optical microscope attached to the system. Peak positions and full widths at half maxima (FWHM) in XRD and Raman spectroscopy measurements are obtained by fitting the data using Gaussian (Lorentzian) functions.[58–60]

An electron transparent MoS_x/hBN/$Al_2O_3(0001)$ sample for cross-sectional transmission electron microscopy (XTEM) measurement is prepared *via* FIB milling carried out in a FEI Nova 600 NanoLab DualBeam SEM/FIB system using 30 kV Ga^+ ions. Prior to milling, the film surface is protected by deposition of a thin, electron beam assisted Pt layer, which also prevents damage from a subsequent deposition of a thicker, ion beam assisted Pt layer, for a total thickness of ~1.5 μm. TEM images of the film are acquired in a JEOL JEM-2800 scanning TEM (S/TEM) operated at 200 kV for imaging.

RESULTS AND DISCUSSION

Figures 1a-c are representative room-temperature LEED patterns obtained *in situ* from (a) bare $Al_2O_3(0001)$ substrate (incident electron energy E = 230 eV), (b) after exposure to borazine (E = 253 eV), and (c) after the deposition of 3-nm-thick MoS_x film (E = 254 eV). Figure 1a shows a six-fold symmetric LEED pattern, characteristic of $Al_2O_3(0001)$-(1×1) unreconstructed surface, indicative of a clean surface.[32] We measure the periodicity of the LEED spots, which is proportional to the reciprocal lattice spacing of $Al_2O_3(0001)$ surface lattice, and use it to calibrate the other LEED patterns and extract in-plane lattice spacings d as described in the Supplementary Information (SI). We observe similar six-fold symmetric LEED patterns (Figs. 1b and c) after the growth of hBN and MoS_x layers. From the diffraction spot spacings , we extract d_{01} values of 2.16 ± 0.06 Å along $[2\bar{1}\bar{1}0]$ for $hBN/Al_2O_3(0001)$ and 2.67 ± 0.08 Å for $MoS_x/hBN/Al_2O_3(0001)$, which are in fair agreement with the d_{01} values of 2.17 Å and 2.73 Å, respectively, expected for hBN(0001) and $MoS_2(0001)$-(1×1) surfaces.[4,9] We note that the LEED pattern (not shown) from a similarly thick MoS_x film grown on bare $Al_2O_3(0001)$, using the same deposition parameters, does not show any diffraction spots.

Figure 1d shows AES data obtained from the same sample after borazine exposure (black curve) and after the deposition of the MoS_x film (red curve). We observe Auger electron peaks at 169 eV, 377 eV, and 503 eV corresponding to boron, nitrogen, and oxygen, respectively, after borazine exposure. The presence of B and N peaks in the AES data is indicative of borazine adsorption on the $Al_2O_3(0001)$ surface and is consistent with the detection of LEED spots characteristic of hBN layer in Fig. 1b. We attribute the O peak in the spectrum to the $Al_2O_3(0001)$ substrate and suggest that the hBN layer is very thin and/or that it does not cover the surface completely. After the deposition of MoS_x film, we observe Auger electron peaks at 118 eV, 185 eV, and 222 eV all due to Mo and at 150 eV due to S. We note that within the detection limits of our measurements, the O signal is absent, indicative of O-free sputter deposition.

Figure 2 shows XPS data obtained from an air-exposed $MoS_x/Al_2O_3(0001)$ sample. We find two S $2p$ peaks, at 161.9 eV due to S $2p_{3/2}$ and at 163.1 eV due to S $2p_{1/2}$, and three peaks due to Mo. With the assumption (justified below) that there are molybdenum oxides (e.g., MoO_2 and MoO_3)

in addition to MoS_x, we fit the three Mo peaks with two sets of Mo $3d_{5/2}$ and Mo $3d_{3/2}$ doublet peaks, colored red and green in the plot. From the red curve, we identify a Mo $3d_{5/2}$ peak at 229.1 eV and a Mo $3d_{3/2}$ peak at 232.2 eV. The green curve fit to the XPS data at higher binding energies shows a Mo $3d_{5/2}$ peak at 232.6 eV and a Mo $3d_{3/2}$ peak at 235.7 eV. Based on the reference values for Mo found in the NIST XPS database,[35] we attribute the Mo $3d$ doublet peaks at lower and higher binding energies to Mo +4 and Mo +6 oxidation states, respectively. The detection of peaks associated with Mo +6 oxidation state suggests the presence of MoO_3. While the Mo +4 peaks are associated with MoS_2 and MoO_2, we cannot determine the exact contributions from MoO_2 to the peak intensities from our XPS data. However, as we show below, we do not observe any peaks corresponding to MoO_2 in XRD and Raman spectra, based on which we assume that the Mo (+4) peaks are all due to MoS_x. From the S and Mo (+4) peaks, we determine the S/Mo ratio x to be 2.0 ± 0.1.

Figures 3a-d are XRD data obtained from the same set of MoS_x thin films grown for $t = 1800$ s on bare $Al_2O_3(0001)$ (black curves) and on hBN/$Al_2O_3(0001)$ (red curves). Figure 3a is a plot of symmetric XRD $2\theta:\omega$ scans from the two samples, with intensities plotted on logarithmic scale. In both the scans, we find highest intensity peaks, labeled **s**, at $2\theta = 41.68°$ due to Al_2O_3 0006 reflections of the single-crystalline α-$Al_2O_3(0001)$ ($R\bar{3}c$) substrate and two relatively weaker intensity peaks at $2\theta = 20.48°$ and $64.52°$, corresponding to forbidden Al_2O_3 0003 and 0009 reflections, respectively.[36] For direct comparison of the relative intensities of the film peaks in both samples, all the intensity values in each of the XRD scans are normalized to the intensity of the Al_2O_3 0006 reflection. The XRD of $MoS_x/Al_2O_3(0001)$ [MoS_x/hBN/$Al_2O_3(0001)$] reveal four film peaks at $2\theta = 14.36°$ [14.36°], 28.94° [28.92°], 44.04° [43.98°], and 59.99° [59.94°]; the XRD of MoS_x/hBN/$Al_2O_3(0001)$ shows an additional peak at $2\theta = 77.26°$, suggestive of highly oriented growth. Based on the peak positions, in comparison with the expected 2θ values for bulk 2H and 3R phases of MoS_2 (see Table I in the SI), we identify the observed peaks as $000l$ reflections with l = 2, 4, 6, 8, and 10 of 2H-MoS_2, indicative of highly 0001-oriented growth. From the $000l$ reflection peak positions, we determine out-of-plane lattice parameters $c = 1.233 \pm 0.0002$ nm [1.234 ± 0.0006 nm] for $MoS_x/Al_2O_3(0001)$ [MoS_x/hBN/$Al_2O_3(0001)$], which are 0.3% [0.4%] larger than $c_o = 1.229$ nm, the value expected for bulk, stoichiometric 2H-MoS_2.[4] (Here, c is the arithmetic average of the values extracted from each of the $000l$ peaks.) Figure 3b shows asymmetric XRD 2θ:ω scans of the $10\bar{1}3$ reflection, with intensities plotted on a linear scale, obtained from the two samples. We find $10\bar{1}3$ reflection peaks at $2\theta = 39.2°$ [39.45°] for $MoS_x/Al_2O_3(0001)$ [MoS_x/hBN/$Al_2O_3(0001)$], from which, using the c values measured from symmetric XRD 2θ:ω scans (Fig. 3a), we determine in-plane lattice parameters a as 0.3197 ± 0.0009 nm [0.3168 ± 0.0005 nm] that are 1.2% [0.3%] larger than the in-plane lattice constant $a_o = 0.3160$ nm of bulk, stoichiometric 2H-MoS_2.[4] Based on the measured lattice parameters, we conclude that the MoS_x crystals on hBN/$Al_2O_3(0001)$ are relatively less distorted compared to those on $Al_2O_3(0001)$.

Figure 3c shows higher magnification plots of 2H-MoS_x 0002 reflection peaks around $2\theta = 14.4°$ in the XRD data (Fig. 3a) from the two samples, superposed for comparison. For MoS_x/hBN/$Al_2O_3(0001)$, 0002 reflection peak intensity is 3.6× times higher than that observed for $MoS_x/Al_2O_3(0001)$]. FWHM of the MoS_x 0002 peaks are 0.56° [0.45°] for the $MoS_x/Al_2O_3(0001)$ [MoS_x/hBN/$Al_2O_3(0001)$] samples. Furthermore, the XRD of MoS_x/hBN/$Al_2O_3(0001)$ shows satellite peaks around the MoS_x 0002 peak; these are Laue oscillations,[37] characteristic of highly ordered crystalline thin films. From the positions of the satellite peaks, we estimate the film thickness t_{film} as 19 ± 1 nm using the relation[37] $t_{film} = \frac{\lambda}{2(sin\ \theta_i - sin\ \theta_{i+1})}$, where $\lambda = 0.154056$ nm is the

X-ray wavelength and θ_i is the angle corresponding to the i^{th} satellite peak adjacent to the 0002 reflection peak. The calculated t_{film} value, as we show below, is in good agreement with the film thickness measured from the XTEM images.

Figure 3d shows ω-rocking curves for the 2H-MoS$_x$ 0002 reflections obtained from MoS$_x$/Al$_2$O$_3$(0001) (black) and MoS$_x$/hBN/Al$_2$O$_3$(0001) (red), superposed with intensities plotted on linear scale. We find ~5× higher intensity and sharper peak for the MoS$_x$ layers on hBN/Al$_2$O$_3$(0001) compared to the peak from MoS$_x$/Al$_2$O$_3$(0001); FWHM of the peaks are 618 arcseconds [140 arcseconds] for MoS$_x$/Al$_2$O$_3$(0001) [MoS$_x$/hBN/Al$_2$O$_3$(0001)]. Our XRD data clearly indicate that the MoS$_x$ layers grown on hBN/Al$_2$O$_3$(0001) are of superior crystalline quality compared to those deposited on bare Al$_2$O$_3$(0001).

Figure 4a is a typical bright field XTEM image of the MoS$_x$ film deposited for t = 1800 s on hBN/Al$_2$O$_3$(0001). We find that the film is ~20 nm thick with fairly smooth surface and interface, consistent with the Laue oscillations observed in Fig. 3c. We observe lamellar structure within the film and lattice fringes in the Al$_2$O$_3$(0001) substrate. (We do not however have any evidence of the hBN layer at the interface.) As we show below, these lamellae are basal planes of MoS$_x$. While most MoS$_x$(0001) layers are aligned nearly parallel to the interface, we find a few that appear wavy, suggestive of relative misorientation along the growth direction. However, we do not see any edge oriented growth, Type I texture,[38] where the basal planes are oriented normal to the interface, over the entire film thickness.

Figures 4b and c are Fourier transforms (FT) of the film and substrate, respectively, obtained from regions highlighted by red and green squares in Fig. 4a. The FT of the film (Fig. 4b) shows a spot pattern that is characteristic of reciprocal space image of (0002) planes with $[2\bar{1}\bar{1}0]$ zone axis (ZA) in a hexagonal lattice.[39] From the measured spot periodicity, we calculate an interplanar spacing $d \approx 0.62$ nm, which is within measurement uncertainties the same as d_{0002}, i.e. $c = 2d_{0002} = 1.24$ nm, of MoS_x. From the observed symmetry in the FT of the corundum-structured $Al_2O_3(0001)$ (Fig. 4c), we determine the ZA to be $[2\bar{1}\bar{1}0]$. From these results, we conclude that the wavy lamellae observed in the XTEM image are 0001 oriented MoS_x layers with the following crystallographic orientation relationship: $(0001)_{MoS_2} \parallel (0001)_{Al_2O_3}$ and $[2\bar{1}\bar{1}0]_{MoS_2} \parallel [2\bar{1}\bar{1}0]_{Al_2O_3}$.

Figures 5a and b are representative Raman and resonant Raman (RR) spectra, respectively, obtained from MoS_x films using 532 nm (2.33 eV) and 633 nm (1.96 eV) wavelength lasers. In both the plots, black and red curves correspond to MoS_x layers on $Al_2O_3(0001)$ and on $hBN/Al_2O_3(0001)$, respectively. In Fig. 5a, we see peaks at 383 cm^{-1} and at 408 cm^{-1} for both the samples; these peak positions are, respectively, comparable to the characteristic, first-order, in-plane vibration mode, E^1_{2g} (382~383 cm^{-1}), and out-of-plane vibration mode, A_{1g} (407~408 cm^{-1}), of bulk, phase-pure 2H-MoS_2.[40–42] FWHM of the E^1_{2g} and A_{1g} mode peaks are, respectively, ~5 cm^{-1} and ~4.4 cm^{-1} [4.2 cm^{-1} and 3.9 cm^{-1}] for $MoS_x/Al_2O_3(0001)$ [$MoS_x/hBN/Al_2O_3(0001)$]. We note that both the Raman peaks are sharper and of higher intensity for MoS_x layers on $hBN/Al_2O_3(0001)$ than on $Al_2O_3(0001)$. Ratios of integrated intensities I of the two modes, $I_{A_{1g}}/I_{E^1_{2g}}$, are ~2.3 [2.5] for $MoS_x/Al_2O_3(0001)$ [$MoS_x/hBN/Al_2O_3(0001)$]. (Here, I is calculated as the area under a given peak.) The reduction in FWHM of the characteristic modes and an increase in $I_{A_{1g}}/I_{E^1_{2g}}$, observed in $MoS_x/hBN/Al_2O_3(0001)$ compared to $MoS_x/Al_2O_3(0001)$, are considered as indicators of improvement in MoS_2 film crystallinity.[43]

In Fig. 5b, we present RR spectra from the same set of samples. For the MoS_x layers on $Al_2O_3(0001)$ [$hBN/Al_2O_3(0001)$], we find two characteristic peaks, E^1_{2g} at ~382 cm^{-1} [384 cm^{-1}] and A_{1g} at ~412 cm^{-1} [408 cm^{-1}], and multiple peaks at ~179 cm^{-1} [181 cm^{-1}], 460 cm^{-1} [464 cm^{-1}], 528 cm^{-1} [532 cm^{-1}], 568 cm^{-1} [570 cm^{-1}], 599 cm^{-1} [603 cm^{-1}], 640 cm^{-1} [642 cm^{-1}], and 820 cm^{-1} [824 cm^{-1}]. The observation of multiple peaks are a result of RR scattering, which occurs when the laser excitation energy (1.96 eV for the 633 nm wavelength) matches the energy for an optical transition in the material; in MoS_2, the direct band gap is ~1.96 eV at the K point in the Brillouin zone.[41,44] RR scattering results in higher signal intensities compared to those obtained with non-resonant Raman and provides information about phonons that are away from the center of the Brillouin zone, for example, near the zone boundary.[45] As a result, RR spectra are sensitive to structural defects and disorder in the material. This is evident in our data (Fig. 5b), which shows differences in peak positions for the MoS_x layers on $Al_2O_3(0001)$ compared to those on hBN/$Al_2O_3(0001)$]; any such differences, if present in Fig. 5a data are not detectable.

The most intense and asymmetric peak seen in our RR spectra is at ~460 cm^{-1} [464 cm^{-1}] for $MoS_x/Al_2O_3(0001)$ [MoS_x/hBN/$Al_2O_3(0001)$]. This particular peak profile has been investigated in earlier RR scattering studies.[44,45] Frey *et al*[45] and Li *et al*[44] have interpreted the asymmetric shape, observed in Raman spectra of bulk MoS_2 single crystal, as a convolution of two peaks – a second-order peak from a longitudinal acoustic (LA) phonon at the M point on the zone boundary, referred to as 2LA(M) at ~454 cm^{-1}, and a first-order optical phonon A_{2u} at ~465 cm^{-1}. From the 2LA(M) mode frequency, first-order LA(M) mode frequency is calculated to be 227 cm^{-1}.[44,45] The LA(M) phonon mode, analogous to the *D* peak of graphene, is reported to be sensitive to defects and imperfections in the MoS_2 crystal lattice.[45–47] Based on this information, we assign phonon modes to each of the peaks observed in our RR spectra as follows: the peak at ~460 cm^{-1} [464 cm^{-1} in case of MoS_x/hBN/$Al_2O_3(0001)$] is due to a combination of 2LA(M) + A_{2u}; the peaks at ~179 cm^{-1} [181 cm^{-1}], 640 cm^{-1} [642 cm^{-1}], and 820 cm^{-1} [824 cm^{-1}] can be assigned to the A_{1g} − LA(M), A_{1g} + LA(M), and 2A_{1g} phonon modes, respectively;[41,44,45] the peaks observed at ~528 cm^{-1} [532 cm^{-1}], 568 cm^{-1} [570 cm^{-1}], and 599 cm^{-1} [603 cm^{-1}] can be assigned to the E_{1g} + LA(M), 2E_{1g}, and E^1_{2g} + LA(M) phonon modes, respectively.[41,45] (The E_{1g} mode, at ~285 cm^{-1}, is a first-order characteristic Raman mode of MoS_2 that is forbidden in a backscattering Raman experiment and hence we do not see it in our data.[45]) Finally, we note the presence of defect-sensitive LA(M) phonon mode peak at ~229 cm^{-1}, clearly visible in the RR spectra of the $MoS_x/Al_2O_3(0001)$ (Fig. 5b, black curve). (This peak is also visible, however at lower intensities, in our Raman spectra obtained using 532 nm wavelength laser.) The absence of this peak in the data from MoS_x/hBN/$Al_2O_3(0001)$ (Fig. 5b, red curve) suggests that the MoS_x layers on hBN/$Al_2O_3(0001)$ are of better crystal quality than on bare $Al_2O_3(0001)$.

The difference in peak positions ($\Delta\omega$) of the E^1_{2g} and A_{1g} first order modes of MoS_2 is used as a measure of film thickness with $\Delta\omega$ around 25 cm^{-1} corresponding to bulk 2H-MoS_2.[44,48] From Fig. 5a, we obtain $\Delta\omega = 25 \pm 1$ cm^{-1} for both sets of MoS_x films. From Fig. 5b, we measure $\Delta\omega = 26 \pm 4$ cm^{-1} [28 ± 4 cm^{-1}] for $MoS_x/Al_2O_3(0001)$ [MoS_x/hBN/$Al_2O_3(0001)$]. The fact that $\Delta\omega \geq 25 \pm 1$ cm^{-1} implies that the MoS_x films are multilayer thick, as expected, and consistent with our XRD and TEM measurements.

In summary, our XPS, XRD, TEM, and Raman spectroscopy results reveal that the as-deposited MoS_x films are nearly stoichiometric, 0001-oriented, and with a relatively larger unit cell volume compared to the bulk 2H-MoS_2. The XRD and Raman spectroscopy data show MoS_x films are more highly ordered, with relatively less lattice distortions and fewer defects on hBN/$Al_2O_3(0001)$ than those on $Al_2O_3(0001)$, indicating that hBN buffer layer improves the crystalline quality of MoS_x layers. These results are qualitatively similar to those reported for the growth of Ta_2C films on hBN/$Al_2O_3(0001)$.[37] While the exact mechanisms leading to the observed enhancement in crystal orientation and quality are not clear, we speculate that surface diffusion of adspecies during deposition is relatively easier on hBN surfaces due to the lack of dangling bonds than on $Al_2O_3(0001)$ surface. This is plausible and consistent with previous demonstrations of vdW epitaxy by Koma and others.[22–28]

CONCLUSIONS

In conclusion, we have demonstrated the growth of highly oriented MoS_x layers ($x = 2.0 \pm 0.1$) on single-crystalline $Al_2O_3(0001)$ and on hBN-covered $Al_2O_3(0001)$ substrates via reactive direct current magnetron sputtering in H_2S/Ar gas mixture. Using *in situ* AES and LEED, we confirm the formation of hBN on $Al_2O_3(0001)$ and MoS_x on hBN. XPS, XRD, TEM, and Raman spectroscopy measurements indicate formation of 0001-oriented 2H-$MoS_{x \approx 2}$ multilayered films and an enhancement in film crystallinity when deposited on hBN/$Al_2O_3(0001)$. We also find, using Raman spectroscopy, the defect sensitive LA(M) Raman mode of MoS_x at ~229 cm^{-1} observed for $MoS_x/Al_2O_3(0001)$ is suppressed in MoS_x/hBN/$Al_2O_3(0001)$. We believe that our findings are of interest in understanding the role of van der Waals materials in heteroepitaxy of crystalline solids.

FIGURES

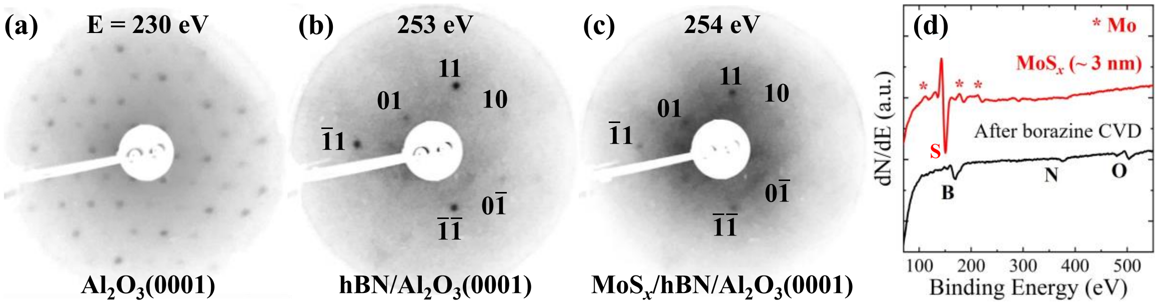

Figure 1. *In-situ* room-temperature low-energy electron diffraction (LEED) patterns obtained using incident electron energies E = 230 eV, 253 eV, and 254 eV, respectively, from (a) bare Al$_2$O$_3$(0001) substrate, (b) after exposure to 1.2×10^5 L of borazine at T_s = 1373 K, followed by (c) reactive sputter deposition of an ≈ 3-nm-thick MoS$_x$ film at T_s = 1073 K. Contrast in the images (b) and (c) has been enhanced to see the LEED spots better. (d) *In-situ* Auger electron spectroscopy (AES) data acquired from the same sample after borazine exposure (black curve) and subsequent MoS$_x$ deposition (red curve).

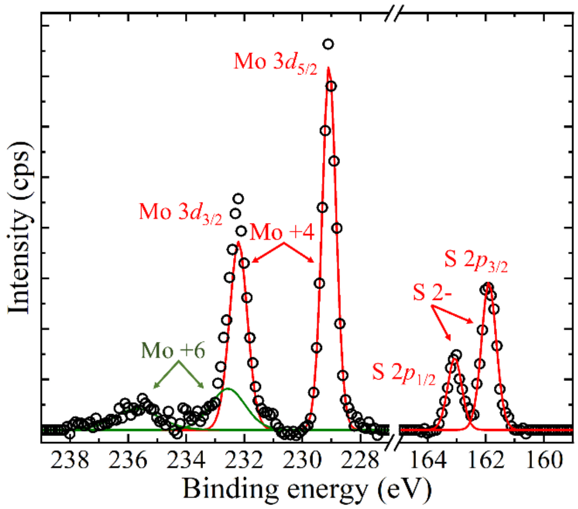

Figure 2. X-ray photoelectron spectra (XPS) around Mo 3*d* and S 2*p* peaks obtained from an air-exposed, ≈ 20-nm-thick, $MoS_x/Al_2O_3(0001)$ film after Shirley background subtraction. Open circles are the raw data, red and green lines are Gaussian fits to MoS_x and MoO_3 peaks, respectively. From the data, we determine S/Mo ratio x to be 2.0 ± 0.1.

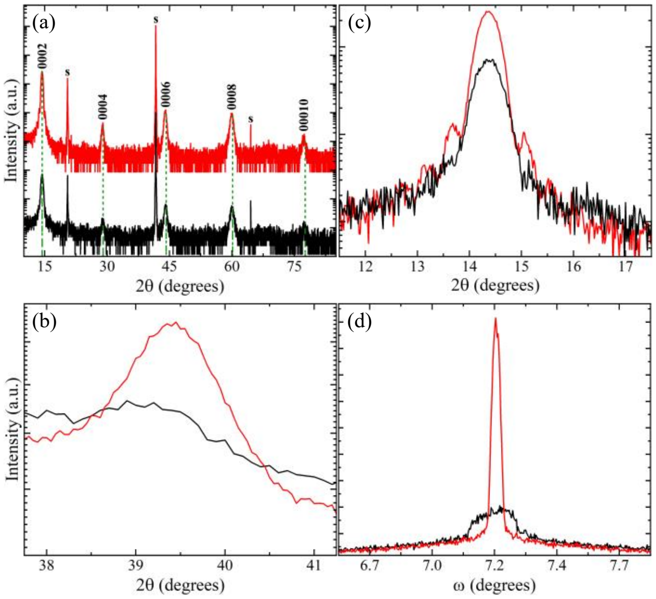

Figure 3. (a-d) X-ray diffraction (XRD) measurements obtained from ≈ 20-nm-thick MoS_x films sputter-deposited on bare $Al_2O_3(0001)$ (black curves) and $hBN/Al_2O_3(0001)$ (red curves) with intensities plotted on (a, c) logarithmic and (b, d) linear scales. (a) Symmetric 2θ:ω scans. **s** refers to Al_2O_3 $000l$ reflections with $l = 3$, 6, and 9 at progressively increasing 2θ values. Peaks due to the film are labeled as shown. Dotted green lines highlight the expected peak positions of stoichiometric 2H-MoS_2 phase.[4] (b) Asymmetric 2θ:ω scans acquired around the MoS_2 $10\bar{1}3$ reflections from the same set of samples at 2θ = 39.2° for $MoS_x/Al_2O_3(0001)$ and 2θ = 39.45° for $MoS_x/hBN/Al_2O_3(0001)$ samples. (c) Magnified view of a portion of the XRD data around MoS_2 0002 reflection (2θ = 14.36°) in (a) from both the samples superposed for comparison. Fringes around the 0002 peak in the red curve are Laue oscillations. (d) ω-rocking curves for the MoS_2 0002 reflections with θ = 7.18° in the two samples.

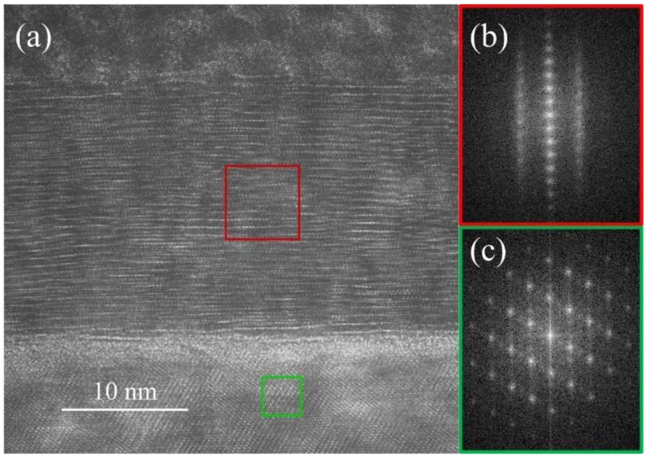

Figure 4. (a) Typical cross-sectional transmission electron microscopy (XTEM) image from a MoS_x/hBN/Al_2O_3(0001) sample showing region around the substrate-film interface. (b, c) Fourier transforms of the regions within the film and the substrate, highlighted by (b) red and (c) green squares, respectively.

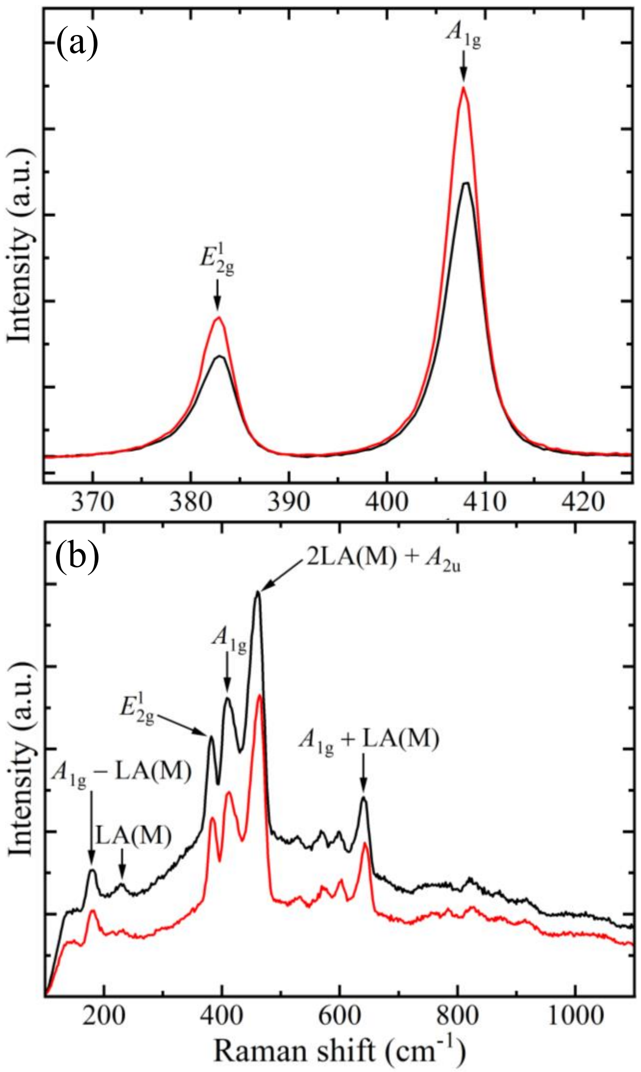

Figure 5. Characteristic Raman spectra obtained from $MoS_x/Al_2O_3(0001)$ (black curve) and $MoS_x/hBN/Al_2O_3(0001)$ (red curve) samples using (a) 532 nm and (b) 633 nm wavelength laser excitations. In both plots, peak intensities are absolute and the data are plotted as obtained without any lateral or vertical translations. First order modes – E^1_{2g} (~383 cm^{-1}) and A_{1g} (~408 cm^{-1}) are seen in both the plots. However, second order modes enhanced by resonant Raman scattering A_{1g} ± LA(M), 2LA(M) + A_{2u} are observed only in (b). The LA(M) mode at ~229 cm^{-1}, associated with defects, is observed in the Raman spectra from $MoS_x/Al_2O_3(0001)$ sample but not in the film grown on $hBN/Al_2O_3(0001)$.

ASSOCIATED CONTENT

Supporting Information

Comparison of XRD peak positions (2θ values in degrees) for symmetric 000*l* reflections obtained from our samples – $MoS_x/Al_2O_3(0001)$, $MoS_x/hBN/Al_2O_3(0001)$ with 2θ values for bulk, phase pure, 2H- and 3R-MoS_2. Details on indexing of low energy electron diffraction patterns.

NOTES

The authors declare no competing financial interests.

ACKNOWLEDGEMENTS

We gratefully acknowledge support from the Air Force Office of Scientific Research (AFOSR, Dr. Ali Sayir) under Grant # FA9550-141-0106, FA9550-18-1-0050 and, FA9550-462 20-1-0184. We thank the Office of Naval Research (Dr. Chagaan Baatar) for the funds received under Grant # N00014-12-1-0518 that were used to build the UHV deposition system. SK thanks the National Science Foundation (NSF) for DMR Award 2211350 (Dr. James Edgar). KT is supported by the Japanese Student Service Organization (L16111111026) and the UCLA Department of Materials Science and Engineering for his doctoral study in the United States. KH is supported by the Japan US Advanced Collaborative Education Program (JUACEP). We thank Professor Abby Kavner for allowing us to use their Raman spectroscopy system and Jan Tesar for acquiring a few of the Raman scans. We thank Mr. Noah Bodzin and the Nanoelectronics Research Facility in the UCLA Henry Samueli School of Engineering for assistance with focused ion beam milling. The authors acknowledge the use of facilities and instrumentation at the UC Irvine Materials Research Institute

(IMRI), which is supported in part by the National Science Foundation through the UC Irvine Materials Research Science and Engineering Center (DMR-2011967).

REFERENCES

(1) Jellinek, F.; Brauer, G.; Muller, H. Molybdenum and Niobium Sulphides. *Nature* **1960**, *185* (4710), 376–377. https://doi.org/10.1038/185376a0.

(2) Dickinson, R. G.; Pauling, L. The Crystal Structure of Molybdenite. *J. Am. Chem. Soc.* **1923**, *45* (6), 1466–1471. https://doi.org/10.1021/ja01659a020.

(3) Schönfeld, B.; Huang, J. J.; Moss, S. C. Anisotropic Mean-square Displacements (MSD) in Single-crystals of 2H- and 3R-MoS2. *Acta Crystallogr. Sect. B* **1983**, *39* (4), 404–407. https://doi.org/10.1107/S0108768183002645.

(4) Bronsema, K. D.; De Boer, J. L.; Jellinek, F. On the Structure of Molybdenum Diselenide and Disulfide. *ZAAC - J. Inorg. Gen. Chem.* **1986**, *540* (9–10), 15–17. https://doi.org/10.1002/zaac.19865400904.

(5) Strachan, J.; Masters, A. F.; Maschmeyer, T. 3R-MoS 2 in Review: History, Status, and Outlook. *ACS Appl. Energy Mater.* **2021**, *4* (8), 7405–7418. https://doi.org/10.1021/acsaem.1c00638.

(6) Kam, K. K.; Parkinson, B. A. Detailed Photocurrent Spectroscopy of the Semiconducting Group VI Transition Metal Dichalcogenides. *J. Phys. Chem.* **1982**, *86* (4), 463–467. https://doi.org/10.1021/j100393a010.

(7) Mak, K. F.; Lee, C.; Hone, J.; Shan, J.; Heinz, T. F. Atomically Thin MoS2: A New Direct-

Gap Semiconductor. *Phys. Rev. Lett.* **2010**, *105* (13), 2–5. https://doi.org/10.1103/PhysRevLett.105.136805.

(8) Elias, C.; Valvin, P.; Pelini, T.; Summerfield, A.; Mellor, C. J.; Cheng, T. S.; Eaves, L.; Foxon, C. T.; Beton, P. H.; Novikov, S. V.; Gil, B.; Cassabois, G. Direct Band-Gap Crossover in Epitaxial Monolayer Boron Nitride. *Nat. Commun.* **2019**, *10* (1), 1–7. https://doi.org/10.1038/s41467-019-10610-5.

(9) Paszkowicz, W.; Pelka, J. B.; Knapp, M.; Szyszko, T.; Podsiadlo, S. Lattice Parameters and Anisotropic Thermal Expansion of Hexagonal Boron Nitride in the 10-297.5 K Temperature Range. *Appl. Phys. A Mater. Sci. Process.* **2002**, *75* (3), 431–435. https://doi.org/10.1007/s003390100999.

(10) Novoselov, K. S.; Mishchenko, A.; Carvalho, A.; Castro Neto, A. H. 2D Materials and van Der Waals Heterostructures. *Science* **2016**, *353* (6298), aac9439. https://doi.org/10.1126/science.aac9439.

(11) Liu, Y.; Weiss, N. O.; Duan, X.; Cheng, H. C.; Huang, Y.; Duan, X. Van Der Waals Heterostructures and Devices. *Nat. Rev. Mater.* **2016**, *1* (9). https://doi.org/10.1038/natrevmats.2016.42.

(12) Geim, A. K.; Grigorieva, I. V. Van Der Waals Heterostructures. *Nature* **2013**, *499* (7459), 419–425. https://doi.org/10.1038/nature12385.

(13) Ajayan, P.; Kim, P.; Banerjee, K. Two-Dimensional van Der Waals Materials. *Phys. Today* **2016**, *69* (9), 38–44. https://doi.org/10.1063/PT.3.3297.

(14) Liu, X.; Hersam, M. C. 2D Materials for Quantum Information Science. *Nat. Rev. Mater.*

2019, *4* (10), 669–684. https://doi.org/10.1038/s41578-019-0136-x.

(15) He, F.; Zhou, Y.; Ye, Z.; Cho, S.-H.; Jeong, J.; Meng, X.; Wang, Y. Moiré Patterns in 2D Materials: A Review. *ACS Nano* **2021**, *15* (4), 5944–5958. https://doi.org/10.1021/acsnano.0c10435.

(16) Shi, Y.; Zhou, W.; Lu, A. Y.; Fang, W.; Lee, Y. H.; Hsu, A. L.; Kim, S. M.; Kim, K. K.; Yang, H. Y.; Li, L. J.; Idrobo, J. C.; Kong, J. Van Der Waals Epitaxy of MoS 2 Layers Using Graphene as Growth Templates. *Nano Lett.* **2012**, *12* (6), 2784–2791. https://doi.org/10.1021/nl204562j.

(17) McCreary, K. M.; Hanbicki, A. T.; Robinson, J. T.; Cobas, E.; Culbertson, J. C.; Friedman, A. L.; Jernigan, G. G.; Jonker, B. T. Large-Area Synthesis of Continuous and Uniform MoS2 Monolayer Films on Graphene. *Adv. Funct. Mater.* **2014**, *24* (41), 6449–6454. https://doi.org/10.1002/adfm.201401511.

(18) Wang, S.; Wang, X.; Warner, J. H. All Chemical Vapor Deposition Growth of MoS2:H-BN Vertical van Der Waals Heterostructures. *ACS Nano* **2015**, *9* (5), 5246–5254. https://doi.org/10.1021/acsnano.5b00655.

(19) Miwa, J. A.; Dendzik, M.; Grønborg, S. S.; Bianchi, M.; Lauritsen, J. V.; Hofmann, P.; Ulstrup, S. Van Der Waals Epitaxy of Two-Dimensional MoS2-Graphene Heterostructures in Ultrahigh Vacuum. *ACS Nano* **2015**, *9* (6), 6502–6510. https://doi.org/10.1021/acsnano.5b02345.

(20) Fu, L.; Fu, L.; Sun, Y.; Wu, N.; Mendes, R. G.; Chen, L.; Xu, Z.; Zhang, T.; Rümmeli, M. H.; Rellinghaus, B.; Pohl, D.; Zhuang, L. Direct Growth of MoS2/h-BN Heterostructures

via a Sulfide-Resistant Alloy. *ACS Nano* **2016**, *10* (2), 2063–2070. https://doi.org/10.1021/acsnano.5b06254.

(21) Xin, W.; Severino, J.; De Rosa, I. M.; Yu, D.; Mckay, J.; Ye, P.; Yin, X.; Yang, J.-M.; Carlson, L.; Kodambaka, S. One-Step Synthesis of Tunable-Size Gold Nanoplates on Graphene Multilayers. *Nano Lett.* **2018**, *18* (3), 1875–1881. https://doi.org/10.1021/acs.nanolett.7b05173.

(22) Koma, A.; Sunouchi, K.; Miyajima, T. Fabrication and Characterization of Heterostructures with Subnanometer Thickness. *Microelectron. Eng.* **1984**, *2* (1–3), 129–136. https://doi.org/10.1016/0167-9317(84)90057-1.

(23) Koma, A.; Yoshimura, K. Ultrasharp Interfaces Grown with Van Der Waals Epitaxy. *Surf. Sci.* **1986**, *174* (1–3), 556–560. https://doi.org/10.1016/0039-6028(86)90471-1.

(24) Saiki, K.; Ueno, K.; Shimada, T.; Koma, A. Application of Van Der Waals Epitaxy to Highly Heterogeneous Systems. *J. Cryst. Growth* **1989**, *95* (1–4), 603–606. https://doi.org/10.1016/0022-0248(89)90475-2.

(25) Ohuchi, F. S.; Parkinson, B. A.; Ueno, K.; Koma, A. Van Der Waals Epitaxial Growth and Characterization of MoSe 2 Thin Films on SnS 2. *J. Appl. Phys.* **1990**, *68* (5), 2168–2175. https://doi.org/10.1063/1.346574.

(26) Koma, A. Van Der Waals Epitaxy—a New Epitaxial Growth Method for a Highly Lattice-Mismatched System. *Thin Solid Films* **1992**, *216* (1), 72–76. https://doi.org/10.1016/0040-6090(92)90872-9.

(27) Löher, T.; Ueno, K.; Koma, A. Van Der Waals Type Buffer Layers: Epitaxial Growth of

the Large Lattice Mismatch System CdS/InSe/H–Si(111). *Appl. Surf. Sci.* **1998**, *130–132*, 334–339. https://doi.org/10.1016/S0169-4332(98)00080-4.

(28) Koma, A. Van Der Waals Epitaxy for Highly Lattice-Mismatched Systems. *J. Cryst. Growth* **1999**, *201–202*, 236–241. https://doi.org/10.1016/S0022-0248(98)01329-3.

(29) Kim, Y.; Cruz, S. S.; Lee, K.; Alawode, B. O.; Choi, C.; Song, Y.; Johnson, J. M.; Heidelberger, C.; Kong, W.; Choi, S.; Qiao, K.; Almansouri, I.; Fitzgerald, E. A.; Kong, J.; Kolpak, A. M.; Hwang, J.; Kim, J. Remote Epitaxy through Graphene Enables Two-Dimensional Material-Based Layer Transfer. *Nature* **2017**, *544* (7650), 340–343. https://doi.org/10.1038/nature22053.

(30) Kong, W.; Li, H.; Qiao, K.; Kim, Y.; Lee, K.; Nie, Y.; Lee, D.; Osadchy, T.; Molnar, R. J.; Gaskill, D. K.; Myers-Ward, R. L.; Daniels, K. M.; Zhang, Y.; Sundram, S.; Yu, Y.; Bae, S. hoon; Rajan, S.; Shao-Horn, Y.; Cho, K.; Ougazzaden, A.; Grossman, J. C.; Kim, J. Polarity Governs Atomic Interaction through Two-Dimensional Materials. *Nat. Mater.* **2018**, *17* (11), 999–1004. https://doi.org/10.1038/s41563-018-0176-4.

(31) Lin, Y. C.; Lu, N.; Perea-Lopez, N.; Li, J.; Lin, Z.; Peng, X.; Lee, C. H.; Sun, C.; Calderin, L.; Browning, P. N.; Bresnehan, M. S.; Kim, M. J.; Mayer, T. S.; Terrones, M.; Robinson, J. A. Direct Synthesis of van Der Waals Solids. *ACS Nano* **2014**, *8* (4), 3715–3723. https://doi.org/10.1021/nn5003858.

(32) Aleman, A.; Li, C.; Zaid, H.; Kindlund, H.; Fankhauser, J.; Prikhodko, S. V.; Goorsky, M. S.; Kodambaka, S. Ultrahigh Vacuum Dc Magnetron Sputter-Deposition of Epitaxial Pd(111)/Al 2 O 3 (0001) Thin Films . *J. Vac. Sci. Technol. A Vacuum, Surfaces, Film.* **2018**,

36 (3), 030602. https://doi.org/10.1116/1.5021609.

(33) Tanaka, K.; Fankhauser, J.; Zaid, H.; Aleman, A.; Sato, M.; Yu, D.; Ebnonnasir, A.; Li, C.; Kobashi, M.; Goorsky, M. S.; Kodambaka, S. Kinetics of Zr-Al Intermetallic Compound Formation during Ultra-High Vacuum Magnetron Sputter-Deposition of Zr/Al2O3(0001) Thin Films. *Acta Mater.* **2018**, *152*, 34–40. https://doi.org/10.1016/j.actamat.2018.04.018.

(34) Tanaka, K.; Aleman, A.; Liao, M. E.; Wang, Y.; Goorsky, M. S.; Kodambaka, S. Effects of Ultra-Low Ethylene Partial Pressure on Microstructure and Composition of Reactively Sputter-Deposited Ta–C Thin Films. *Thin Solid Films* **2019**, *688* (July), 137440. https://doi.org/10.1016/j.tsf.2019.137440.

(35) *NIST X-ray Photoelectron Spectroscopy Database, Version 4.1 (National Institute of Standards and Technology, Gaithersburg, 2012)*. http://srdata.nist.gov/xps/. https://doi.org/10.18434/T4T88K.

(36) Tanaka, K.; Aleman, A.; Zaid, H.; Liao, M. E.; Hojo, K.; Wang, Y.; Goorsky, M. S.; Kodambaka, S. Ultra-High Vacuum Dc Magnetron Sputter-Deposition of 0001-Textured Trigonal α-Ta2C/Al2O3(0001) Thin Films. *Materialia* **2020**, *13*, 100838. https://doi.org/10.1016/j.mtla.2020.100838.

(37) Tanaka, K.; Arias, P.; Hojo, K.; Liao, M. E.; Aleman, A.; Zaid, H.; Goorsky, M. S.; Kodambaka, S. Synergistic van Der Waals Epitaxy and Remote Epitaxy : An Approach to Superior Quality Crystal Growth (to Be Published).

(38) Moser, J.; Liao, H.; Levy, F. Texture Characterisation of Sputtered MoS 2 Thin Films by Cross-Sectional TEM Analysis. *J. Phys. D. Appl. Phys.* **1990**, *23* (5), 624–626.

https://doi.org/10.1088/0022-3727/23/5/026.

(39) Williams, D. B.; Carter, C. B. Obtaining and Indexing Parallel-Beam Diffraction Patterns. In *Transmission Electron Microscopy*; Springer US: Boston, MA, 2009; pp 283–309. https://doi.org/10.1007/978-0-387-76501-3_18.

(40) Lee, J. U.; Kim, K.; Han, S.; Ryu, G. H.; Lee, Z.; Cheong, H. Raman Signatures of Polytypism in Molybdenum Disulfide. *ACS Nano* **2016**, *10* (2), 1948–1953. https://doi.org/10.1021/acsnano.5b05831.

(41) Windom, B. C.; Sawyer, W. G.; Hahn, D. W. A Raman Spectroscopic Study of MoS 2 and MoO 3: Applications to Tribological Systems. *Tribol. Lett.* **2011**, *42* (3), 301–310. https://doi.org/10.1007/s11249-011-9774-x.

(42) Verble, J. L.; Wieting, T. J. Lattice Mode Degeneracy in MoS2 and Other Layer Compounds. *Phys. Rev. Lett.* **1970**, *25* (6), 362–365. https://doi.org/10.1103/PhysRevLett.25.362.

(43) McDevitt, N. T.; Zabinski, J. S.; Donley, M. S. The Use of Raman Scattering to Study Disorder in Pulsed Laser Deposited MoS2 Films. *Thin Solid Films* **1994**, *240* (1–2), 76–81. https://doi.org/10.1016/0040-6090(94)90698-X.

(44) Li, H.; Zhang, Q.; Yap, C. C. R.; Tay, B. K.; Edwin, T. H. T.; Olivier, A.; Baillargeat, D. From Bulk to Monolayer MoS 2: Evolution of Raman Scattering. *Adv. Funct. Mater.* **2012**, *22* (7), 1385–1390. https://doi.org/10.1002/adfm.201102111.

(45) Frey, G. L.; Tenne, R.; Matthews, M. J.; Dresselhaus, M. S.; Dresselhaus, G. Raman and Resonance Raman Investigation of MoS2 Nanoparticles. *Phys. Rev. B - Condens. Matter*

Mater. Phys. **1999**, *60* (4), 2883–2892. https://doi.org/10.1103/PhysRevB.60.2883.

(46) McDevitt, N. T.; Zabinski, J. S.; Donley, M. S.; Bultman, J. E. Disorder-Induced Low-Frequency Raman Band Observed in Deposited MoS 2 Films . *Appl. Spectrosc.* **1994**, *48* (6), 733–736. https://doi.org/10.1366/000370294774369063.

(47) Mignuzzi, S.; Pollard, A. J.; Bonini, N.; Brennan, B.; Gilmore, I. S.; Pimenta, M. A.; Richards, D.; Roy, D. Effect of Disorder on Raman Scattering of Single-Layer Mo S2. *Phys. Rev. B - Condens. Matter Mater. Phys.* **2015**, *91* (19), 1–7. https://doi.org/10.1103/PhysRevB.91.195411.

(48) Lee, C.; Yan, H.; Brus, L. E.; Heinz, T. F.; Hone, J.; Ryu, S. Anomalous Lattice Vibrations of Single- and Few-Layer MoS2. *ACS Nano* **2010**, *4* (5), 2695–2700. https://doi.org/10.1021/nn1003937.

(49) Arias, P.; Ebnonnasir, A.; Ciobanu, C. V; Kodambaka, S. Growth Kinetics of Two-Dimensional Hexagonal Boron Nitride Layers on Pd(111). *Nano Lett.* **2020**, *20* (4), 2886–2891. https://doi.org/10.1021/acs.nanolett.0c00704.

(50) Arias, P.; Abdulslam, A.; Ebnonnasir, A.; Ciobanu, C. V; Kodambaka, S. Bifurcation and Orientation-Dependence of Corrugation of 2D Hexagonal Boron Nitride on Palladium. *2D Mater.* **2018**, *5* (4), 045001. https://doi.org/10.1088/2053-1583/aacd71.

(51) Stock, A.; Pohland, E. Borwasserstoffe, IX.: B 3 N 3 H 6. *Ber. dtsch. Chem. Ges. A/B* **1926**, *59* (9), 2215–2223. https://doi.org/10.1002/cber.19260590907.

(52) Baker, M. .; Gilmore, R.; Lenardi, C.; Gissler, W. XPS Investigation of Preferential Sputtering of S from MoS2 and Determination of MoSx Stoichiometry from Mo and S Peak

Positions. *Appl. Surf. Sci.* **1999**, *150* (1–4), 255–262. https://doi.org/10.1016/S0169-4332(99)00253-6.

(53) Greczynski, G.; Kindlund, H.; Petrov, I.; Greene, J.; Hultman, L. Sputter-Cleaned Epitaxial VxMo(1-x)Ny/MgO(001) Thin Films Analyzed by X-Ray Photoelectron Spectroscopy: 2. Single-Crystal V0.47Mo0.53N0.92. *Surf. Sci. Spectra* **2013**, *20* (1), 74–79. https://doi.org/10.1116/11.20130601.

(54) Greczynski, G.; Kindlund, H.; Petrov, I.; Greene, J.; Hultman, L. Sputter-Cleaned Epitaxial VxMo(1-x)Ny/MgO(001) Thin Films Analyzed by X-Ray Photoelectron Spectroscopy: 3. Polycrystalline V0.49Mo0.51N1.02. *Surf. Sci. Spectra* **2013**, *20* (1), 80–85. https://doi.org/10.1116/11.20130602.

(55) Greczynski, G.; Kindlund, H.; Petrov, I.; Greene, J.; Hultman, L. Sputter-Cleaned Epitaxial VxMo(1-x)Ny/MgO(001) Thin Films Analyzed by X-Ray Photoelectron Spectroscopy: 1. Single-Crystal V0.48Mo0.52N0.64. *Surf. Sci. Spectra* **2013**, *20* (1), 68–73. https://doi.org/10.1116/11.20130301.

(56) Fairley, N.; Fernandez, V.; Richard-Plouet, M.; Guillot-Deudon, C.; Walton, J.; Smith, E.; Flahaut, D.; Greiner, M.; Biesinger, M.; Tougaard, S.; Morgan, D.; Baltrusaitis, J. Systematic and Collaborative Approach to Problem Solving Using X-Ray Photoelectron Spectroscopy. *Appl. Surf. Sci. Adv.* **2021**, *5*, 100112. https://doi.org/10.1016/j.apsadv.2021.100112.

(57) Shirley, D. A. High-Resolution X-Ray Photoemission Spectrum of the Valence Bands of Gold. *Phys. Rev. B* **1972**, *5* (12), 4709–4714. https://doi.org/10.1103/PhysRevB.5.4709.

(58) Yan, R.; Simpson, J. R.; Bertolazzi, S.; Brivio, J.; Watson, M.; Wu, X.; Kis, A.; Luo, T.; Hight Walker, A. R.; Xing, H. G. Thermal Conductivity of Monolayer Molybdenum Disulfide Obtained from Temperature-Dependent Raman Spectroscopy. *ACS Nano* **2014**, *8* (1), 986–993. https://doi.org/10.1021/nn405826k.

(59) Wang, Y.; Cong, C.; Qiu, C.; Yu, T. Raman Spectroscopy Study of Lattice Vibration and Crystallographic Orientation of Monolayer MoS 2 under Uniaxial Strain. *Small* **2013**, *9* (17), 2857–2861. https://doi.org/10.1002/smll.201202876.

(60) Chakraborty, B.; Matte, H. S. S. R.; Sood, A. K.; Rao, C. N. R. Layer-Dependent Resonant Raman Scattering of a Few Layer MoS 2. *J. Raman Spectrosc.* **2013**, *44* (1), 92–96. https://doi.org/10.1002/jrs.4147.

FOR TABLE OF CONTENTS ONLY